The Astrophysical Journal, 864:19 (14pp), 2018 September 1 https://doi.org/10.3847/1538-4357/aad333

Nonthermal Emission from Stellar Bow Shocks

M. V. del Valle[1] and M. Pohl[1,2]
[1] Institute of Physics and Astronomy, University of Potsdam D-14476 Potsdam, Germany; mdvalle@uni-potsdam.de
[2] DESY Platanenallee 6, D-15738 Zeuthen, Germany
Received 2018 May 8; revised 2018 July 10; accepted 2018 July 10; published 2018 August 27

Abstract

Since the detection of nonthermal radio emission from the bow shock of the massive runaway star BD +43°3654, simple models have predicted high-energy emission, at X-rays and gamma-rays, from these Galactic sources. Observational searches for this emission so far give no conclusive evidence but a few candidates at gamma-rays. In this work we aim at developing a more sophisticated model for the nonthermal emission from massive runaway star bow shocks. The main goal is to establish whether these systems are efficient nonthermal emitters, even if they are not strong enough yet to be detected. For modeling the collision between the stellar wind and the interstellar medium we use 2D hydrodynamic simulations. We then adopt the flow profile of the wind and the ambient medium obtained with the simulation as the plasma state for solving the transport of energetic particles injected in the system, as well as the nonthermal emission they produce. For this purpose we solve a 3D (two spatial + energy) advection-diffusion equation in the test-particle approximation. We find that a massive runaway star with a powerful wind converts 0.16%–0.4% of the power injected in electrons into nonthermal emission, mostly produced by inverse Compton scattering of dust-emitted photons by relativistic electrons, and second by synchrotron radiation. This represents a fraction of $\sim 10^{-5}$ to 10^{-4} of the wind kinetic power. Given the better sensibility of current instruments at radio wavelengths, these systems are more prone to be detected at radio through the synchrotron emission they produce rather than at gamma energies.

Key words: gamma-rays: stars – hydrodynamics – radiation mechanisms: nonthermal – stars: winds, outflows

1. Introduction

Runaway massive stars are stars with high spatial velocities ($V_\star > 30$ km s^{-1}) that have been expelled from their formation sites (e.g., Hoogerwerf et al. 2000; Tetzlaff et al. 2011). Massive stars have strong winds that interact with the interstellar medium (ISM) as the stars move supersonically through it. In this interaction a bow shock is formed, in some cases detectable in the infrared (IR; e.g., van Buren & McCray 1988; Kobulnicky et al. 2010). This last emission is reprocessed stellar light by the dust swept by the bow shock. There are of the order of ∼700 stellar bow shocks cataloged so far (Peri et al. 2012, 2015; Kobulnicky et al. 2016).

The bow shock of the massive runaway star BD +43°3654 was detected at radio wavelengths, and the emission might be synchrotron radiation (Benaglia et al. 2010). This suggests that a population of high-energy electrons is present in the source, interacting locally with the magnetic field. In the collision between the ISM and the stellar wind a system of two shocks is formed: a forward shock and a reverse shock. This last shock is adiabatic and fast, with velocities of the order of $\sim 10^3$ km s^{-1}. Hence, it is straightforward to think that this reverse shock might accelerate particles up to high energies through diffusive shock acceleration (DSA).

If the electrons that produce the radio nonthermal emission were accelerated in the reverse shock of BD +43°3654, then they are expected to further interact with the ambient fields: the density and the photons producing high-energy emission via relativistic bremsstrahlung and inverse Compton (IC) scattering. With this in mind, a number of initial models predict nonthermal emission, mainly via IC scattering of IR photons, at X-rays and gamma-rays (del Valle & Romero 2012, 2014; Pereira et al. 2016); see also del Palacio et al. (2018) for a multizone model. López-Santiago et al. (2012) claimed to find the first nonthermal X-ray emission from the bow shock of AE Aurigae; however, later it was demonstrated that the emission is not positionally coincident with that of the AE Aurigae bow shock (Toalá et al. 2017). Nolan et al. (2012) found an unidentified *Fermi* source locally coincident with the position of the bow shock of the massive star H3D 195592, and del Valle et al. (2013) studied the possibility that this gamma emission was being produced in the bow shock. Although theoretically plausible, in the second *Fermi* catalog this source was reclassified as a pulsar (Abdo et al. 2013).

Several searches for high-energy emission from bow shocks of massive runaway stars have followed. At X-rays, these searches were done using both *XMM-Newton* archived observations (Toalá et al. 2017, 2016) and dedicated observations (De Becker et al. 2017), where no nonthermal extended emission was found. De Becker et al. (2017) used the derived upper limits at X-rays and those available at radio wavelength to fit general physical parameters of the sources with a simple model for the nonthermal emission. They found reasonable fit values for four out of the five targets of the sample. Also, making energetic assumptions for all the bow shocks listed in the E-BOSS catalog, they concluded that a clear identification of nonthermal X-ray emission from massive runaway bow shocks requires one order of magnitude (or higher) sensitivity improvement with respect to present observatories.

At gamma-ray wavelengths Schulz et al. (2014) searched for emission in *Fermi* archive data of the 28 bow shocks listed in the E-BOSS catalog (Peri et al. 2012). From the modeled sources only ζ Oph was detectable; however, no emission locally coincident with this source was found in the data; from this it can be concluded that the model predictions were overestimated at least by a factor of ∼5. For the rest of the sources upper limits were derived in the energy range from 100 MeV to 300 GeV. A study of the same sources was made

by the H.E.S.S. Collaboration in the energy range between 0.14 and 18 TeV (H.E.S.S. Collaboration et al. 2018). No associated emission was found, but from the resulting upper limits a constraint on the very high energy emission was obtained: it should be less than 0.1 to 1% of the kinetic wind energy. Recently, Sánchez-Ayaso et al. (2018) presented two runaway stars (Lambda Cephei and LS 2355) whose bow shocks are coincident with two unidentified *Fermi* gamma-ray sources from the third *Fermi* 3FGL catalog (Acero et al. 2015). After cross-correlation between different catalogs at distinct wavelengths, the authors found that these bow shocks are the most peculiar objects in the *Fermi* position ellipses. Using a simple model for estimating the IC emission, they fitted the *Fermi* data for both sources, obtaining reasonable values for the fitted parameters. This makes these systems promising candidates for gamma-ray bow shocks.

The growing observational base and the progressive interest of the gamma-ray and X-ray community on searching nonthermal emission from stellar sources, together with the new observational upper limits, demand now more accurate models of nonthermal emission from runaway star bow shocks. Here we present such a model, aiming to establish new theoretical predictions on nonthermal emission from these sources and also to establish whether these systems can be efficient nonthermal emitters. Detailed theoretical work will help to guide the search of these sources at radio and high energies.

In this work we implement a hydrodynamic code to simulate the interaction of the wind of high-mass runaway stars with the ambient medium, and then we calculate the nonthermal emission associated with this interaction. Assuming that electrons and protons are accelerated via DSA in the reverse shock, we solve the transport of particles and their emissions obtaining emission maps and spectral energy distributions (SEDs). Here we do not focus on any particular source; this will be addressed in future works.

In the next section we give a general introduction to the model, followed by a more detailed description of the hydrodynamics of the wind+ISM interaction and our implementation in Section 3. In Section 4 we present our model for solving the transport of energetic particles. In Section 5 the obtained results are shown, in Section 6 we present a discussion, and in Section 7 we give our conclusions.

2. Introduction to the Model

As mentioned above, the bow shock of a massive runaway star is formed by the collision of the stellar powerful wind with the incoming ISM, in the star's reference frame. The wind and ISM pressure balance at the contact discontinuity. The characteristic scale of the system is usually taken as the standoff distance R_0, given by the balance of the wind and ambient medium ram pressures:

$$R_0 = \sqrt{\frac{\dot{M}_{\rm w} V_{\rm w}}{4\pi \rho_{\rm ISM} v_\star^2}}, \quad (1)$$

where $\dot{M}_{\rm w}$ and $V_{\rm w}$ are the wind mass-loss rate and velocity, respectively, $\rho_{\rm ISM}$ is the ISM density, and $v_\star$ is the star's velocity. In the *instantaneous cooling* approximation R_0 would directly give the distance from the star to the apsis of the bow shock; however, in a real system this distance might vary, due to thermal conduction and cooling, for example (e.g., Raga et al. 1997; Comeron & Kaper 1998; Meyer et al. 2014).

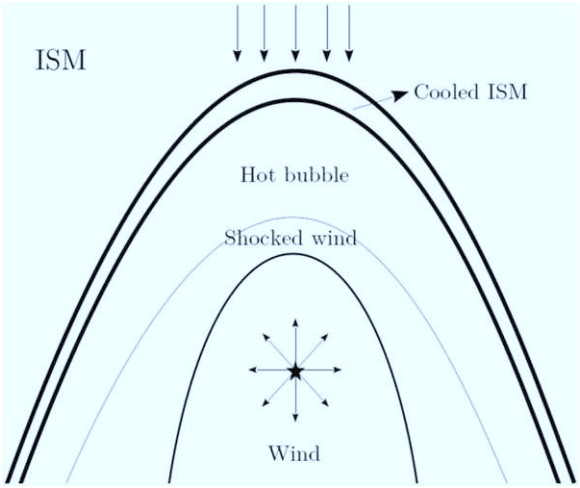

Figure 1. Scheme of a runaway massive star bow shock. Five regions can be distinguished: free-flowing stellar wind, the shocked wind, hot shocked ISM, cooled ISM, and the ISM itself. Due to thermal conduction, two layers of shocked ISM are formed: a hot and low-density layer adjacent to the contact discontinuity, and an outer one formed of cooled, shocked ambient medium (Comeron & Kaper 1998; Meyer et al. 2014).

In the literature a number of works exist on the collision of two fluids and specifically for modeling the bow shocks of massive runaways (e.g., Canto et al. 1996; Wilkin 1996; Raga et al. 1997; Comeron & Kaper 1998; Wilkin 2000; van Marle et al. 2011; Meyer et al. 2014, 2016, 2017). A precise description of the phenomenology requires a dynamical treatment implementing numerical simulations. An appropriate treatment of the hydrodynamics of stellar winds should include both optically thin cooling and thermal conduction (e.g., Raga et al. 1997; Comeron & Kaper 1998).

After the formation of the bow shock, the system would reach globally a steady state. A general sketch of a bow shock is shown in Figure 1. The system is very prone to suffer many instabilities: Rayleigh–Taylor between the dense cooled layer and the hotter less dense one, an instability arising in shocked layers bounded by thermal pressure on one side and ram pressure on the other (e.g., Ryu & Vishniac 1987; Mac Low & Norman 1993; Comeron & Kaper 1998), and Kelvin–Helmholtz owing to the velocity shear between the material layers (e.g., Dgani et al. 1996). A complete analysis of these instabilities is made in Comeron & Kaper (1998).

In this work we use the PLUTO code (Mignone et al. 2007) to solve the 2D hydrodynamic equations following the setup by Meyer et al. (2014; see also Meyer et al. 2016, 2017). At this stage we do not consider the magnetic field in the simulations. As the system reaches a steady state, we use that state as a scenario to solve in it the transport of energetic particles, assumed to be accelerated via DSA in the wind shock. We search for the reverse shock position and inject relativistic electrons and protons there; using our own code, we solve the diffusion–advection equation for the particles in the 2D domain.

The energetic particles would interact with the magnetic field producing synchrotron emission (only for electrons, proton synchrotron is very inefficient in this case), with the density producing relativistic bremsstrahlung and $p-p$ inelastic collisions—for electrons and protons, respectively—and with

the radiation fields: the stellar photon field and the stellar-reprocessed dust emission. Only electrons interact efficiently with the radiation fields, via IC scattering.

Other works that solve the hydrodynamic and magneto-hydrodynamic equations together with the transport of high-energy particles exist. For example, de la Cita et al. (2016) use a similar approach to the one we use, but here we do solve the spatial diffusion of the particles, which is key in the system we are studying. Pakmor et al. (2016) solve the hydrodynamics of galactic winds and cosmic-ray diffusion, but they consider the latter component as a fluid, without solving the energy dependence of the particles, needed to compute the nonthermal emission; in contrast to this system, the pressure of the energetic particles is negligible in our case. Brose et al. (2016) make a self-consistent treatment of the plasma dynamics, acceleration, and transport of cosmic rays in supernova remnants. However, their 1D treatment is not appropriate in our problem.

In the following sections we describe with more detail the hydrodynamic model and the modeling of the transport of relativistic particles.

3. Hydrodynamic Modeling

As mentioned previously, we use the PLUTO code to solve the 2D hydrodynamic equations following the setup by Meyer et al. (2014). We consider a 2D cylindrical coordinate system with coordinates (r, z). The system of equations is the following:

$$\begin{aligned}
&\frac{\partial \rho}{\partial t} + \boldsymbol{v}\cdot\boldsymbol{\nabla}\rho + \rho(\boldsymbol{\nabla}\cdot\boldsymbol{v}) = 0,\\
&\frac{\partial \boldsymbol{v}}{\partial t} + \boldsymbol{v}\cdot\boldsymbol{\nabla}\boldsymbol{v} + \frac{\boldsymbol{\nabla} p}{\rho} = 0,\\
&\frac{\partial p}{\partial t} + \boldsymbol{v}\cdot\boldsymbol{\nabla} p + \rho c_s^2\,\boldsymbol{\nabla}\cdot\boldsymbol{v} = (\gamma_{\rm g}-1)[\Phi(T,\rho) + \boldsymbol{\nabla}\cdot\boldsymbol{F}_{\rm c}].
\end{aligned} \tag{2}$$

Here $\boldsymbol{v}$, ρ, and p are the fluid velocity, its density, and its pressure, respectively; $\gamma_{\rm g} = 5/3$ is the ratio of specific heats for a monoatomic ideal gas; c_s is the sound speed; Φ represents the radiative energy gains (heating) and losses (cooling); and $\boldsymbol{F}_{\rm c}$ is the heat flux due to thermal conduction.

The total density is $\rho = \mu n m_{\rm H}$, with n the total number density and $\mu = 0.61$, the mean molecular weight for a fully ionized medium.[3] The temperature T as a function of density and pressure is given by $T = \mu(m_{\rm H}/k_{\rm B})(p/\rho)$, with $k_{\rm B}$ the Boltzmann constant.

The radiative term Φ can be written as $\Phi(T,\rho) = n_{\rm H}^2\Gamma_\alpha(T) - n_{\rm H}^2\Lambda(T)$, where Γ_α represents the heating and Λ the optically thin cooling, $n_{\rm H}$ is the hydrogen number density, and we consider solar abundances. The cooling term includes the cooling of hydrogen, helium, and metals (tabulated from Wiersma et al. 2009); hydrogen recombination; and forbidden lines collisionally exited. The heating term is due to recombination of hydrogen ions. For further details the reader is referred to Meyer et al. (2014) and references therein.

[3] It is shown in Meyer et al. (2014) that for a massive main-sequence star the Strömgren sphere is greater than the typical scale of the bow shock. Hence, we assume here a fully ionized plasma.

The heat flux $\boldsymbol{F}_{\rm c} = -\kappa\,\boldsymbol{\nabla}T$ is due to thermal conduction. The classical heat flux given by Spitzer's coefficient in a fully ionized plasma is $\kappa = 5.6\times10^{-7}\,T^{5/2}\ {\rm erg\,s^{-1}\,cm^{-1}}$.

3.1. Initial Conditions

We are interested in massive runaway stars with powerful winds, so we consider a typical runaway of mass $M_\star = 40\,M_\odot$, $T_{\rm eff} = 4.25\times10^4$ K, $R_\star = 10^{12}$ cm, $\dot{M}_{\rm w} = 7\times10^{-7}\,M_\odot\ {\rm yr^{-1}}$, $V_{\rm w} = 2000\ {\rm km\,s^{-1}}$, and $V_{\rm star} = 40\ {\rm km\,s^{-1}}$. With these values $R_0 \sim 2.2$ pc.

We use a rectangular box of size $[0,\ 24\,{\rm pc}]\times[-18,\ 8\,{\rm pc}]$ and resolution (880×960). Initially the box is filled with ISM of density $n_{\rm ISM} = 0.57$ and $T = 8000$ K, and velocity $\boldsymbol{v} = -v_\star\hat{k}$. The wind is constantly injected in a region $R^2 = r^2 + z^2 < 1$ pc centered at the origin. Its density is given by $\rho_{\rm w} = \dot{M}_{\rm w}/(4\pi v_{\rm w}R^2)$. We use a tracer (passive scalar) to *color* the wind material. After $\sim16t_{\rm cross}$, with $t_{\rm cross} = R/v_\star$, the expanding bubble turns into a steady bow shock (Meyer et al. 2014).

3.2. Boundary Conditions

In the initial r boundary, because of the symmetry of the problem, we consider axisymmetric boundary conditions. For the end boundary of both r and z we use *outflow* conditions. Also, we do not allow inflow at the z-lower boundary. In the initial z boundary the condition that fresh ISM enters with $\boldsymbol{v} = -v_\star\hat{k}$ is imposed.

For solving the dynamic evolution we use a Runge–Kutta algorithm of third order, with linear spatial reconstruction. These systems are highly prone to instabilities; hence, fluxes are computed using a simple Lax–Friedrichs scheme. This also avoids 2D effects in the symmetry axis. The parabolic term (thermal conduction) is solved using the Super-Time-Stepping scheme implemented in the code.

3.3. Results

In Figure 2 we show the evolution of the density in the simulation domain from $t = 0.3$ to 1.5 Myr, when the large structure has already reached a steady state. Initially the material expands spherically, and the shocked ISM starts to flow surrounding the expanding wind. A thin layer of cooled ISM material starts to form. The structure shows some *fingers* in the hot–cool shocked ISM interface, possibly due to Rayleigh–Taylor instability. At later times some instabilities in the wind–shocked wind interface appear, possibly due to shear (Kelvin–Helmholtz instability), produced by the different velocities of the two layers (see also Figure 3). Comparing the bow shock shape from $t = 0.9$ Myr with that at $t = 1.5$ Myr, we can see that there are few changes in the structure, only in the inner cooling layer owing to instabilities; at $t = 1.5$ Myr the system has already reached a steady state.

In the top panel of Figure 3 we show a map of the velocity at $t = 1.5$ Myr. The highest velocities, $\sim10^3\ {\rm km\,s^{-1}}$, correspond to the wind; the shocked ISM flows with velocities of the order of hundreds of kilometers per second or less. In the bottom panel we show the temperature map, at the same snapshot. The highest temperature corresponds to the shocked wind, with $T\sim7\times10^7$ K . Given the relation $T = 2\times10^{-9}\,V_{\rm shock}^2$ K for an adiabatic shock of velocity $V_{\rm shock}$, this implies a shock velocity $V_{\rm shock}\sim2\times10^3\ {\rm km\,s^{-1}}\sim V_{\rm w}$.

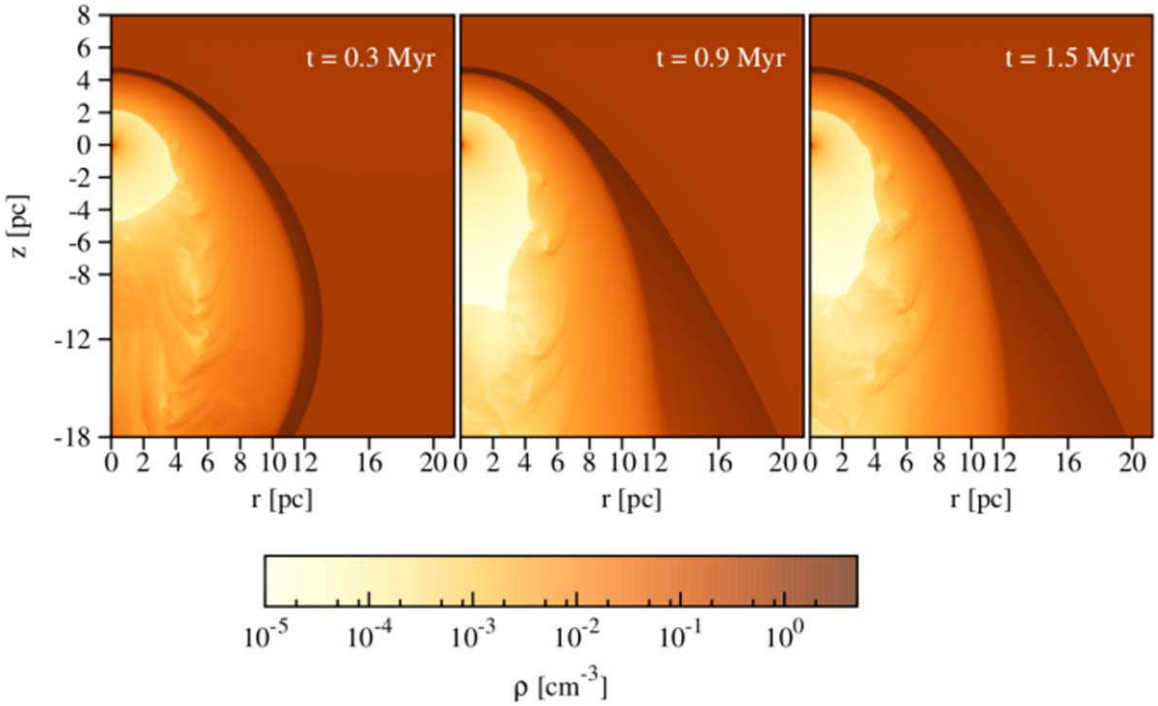

Figure 2. Density maps at different computational times for the interaction of a stellar wind with incoming ISM at a velocity $-v_\star$. Time evolves from left to right.

Comparing the cooling time $t_{\rm cool} = \frac{P}{(\gamma_g - 1)\Lambda(T) n_H^2}$ with the dynamical time of a specific layer $t_{\rm dyn} = \Delta z/v$ establishes the adiabatic/radiative nature of a shock. For the wind shock $T \sim 7 \times 10^7$ K, $n \sim 10^{-4}$ cm^{-3}, $\Lambda(T) \sim 10^{-22}$ erg cm^{-3} s^{-1}, which gives $t_{\rm cool} = 2 \times 10^2$ Gyr $\gg t_{\rm dyn} = 0.2$ kyr, with $\Delta z \sim 0.1$ pc. For the forward shock $T \sim 10^5$ K, $n \sim 0.5$ cm^{-3}, $\Lambda(T) \sim 10^{-21}$ erg cm^{-3} s^{-1}, $t_{\rm cool} = 10$ kyr, which dominates over the dynamical time, which is, for $\Delta z = 0.6$ pc, $t_{\rm dyn} = 0.2$ Myr. Hence, the shock in the wind is adiabatic, and the shock in the ISM is radiative.

Profiles of density and temperature for $r = 0$, $z \geqslant 0$ are shown in Figure 4, at $t = 1.5$ Myr. The density decreases radially as expected from $\rho_{\rm w} \propto R^{-2}$, and a density jump occurs at $z \sim 2.16$ pc that coincides with a jump in the temperature: this is the wind or reverse shock. The contact discontinuity, marked in the figure with a solid vertical line, is located at $z \sim 2.3$ pc, a bit farther than the position predicted theoretically, i.e., $z \sim R_0$, an effect expected by thermal conduction (e.g., Comeron & Kaper 1998). The density increases slowly after the jump. This increase of mass in the intermediate-density layer is caused by thermal conduction (van Buren & McCray 1988). At $z \sim 4.9$ pc another jump in density is encountered, again in the company of a jump in temperature; this is the forward shock. The dense layer of the bow shock is in thermal equilibrium with the ISM.

It is worth mentioning that this profile differs from the more sharply structured typical reverse shock–contact discontinuity–forward shock profile in which the regions of different materials are well delimited. The presence of thermal conduction produces an intermediate-density layer. The temperature of the shocked ambient gas is much lower than that of the shocked wind, which causes a flow of energy outward; in turn, an inward flow of matter from the dense layer into the shocked wind region occurs (Comeron & Kaper 1998).

Meyer et al. (2017) demonstrated that the presence of an ISM magnetic field does not change the global shape of the bow shock, but it modifies the thermal conduction and hence the hot bubble size. The magnetohydrodynamic treatment will be addressed in a future work. Analyzing deeply the hydrodynamics of the system is not the goal of this work; many previous works—mentioned in Section 2—have done this extensively, and the readers are referred to them for further inquiries into the subject.

4. Transport of High-energy Particle Modeling

We solve the transport of electrons and protons in the bow shock of the massive star described in the previous section, using the solution of the HD simulations at $t = 1.5$ Myr. We use the same cylindrical coordinate system (r, z). The diffusion–advection equation for relativistic protons and electrons that follows $N(t, E, \boldsymbol{r}) \equiv$ number of particles/unit energy $\times$ unit volume is

$$\frac{\partial N(t, E, \boldsymbol{r})}{\partial t} = \nabla(D(t, E, \boldsymbol{r})\nabla N(t, E, \boldsymbol{r})) - \nabla(\boldsymbol{v}(t, \boldsymbol{r})N(t, E, \boldsymbol{r})) - \frac{\partial}{\partial E}(P(t, E, \boldsymbol{r})N(t, E, \boldsymbol{r})) + Q(t, E, \boldsymbol{r}), \quad (3)$$

where the first term represents the diffusion in space with diffusion coefficient $D(t, E, \boldsymbol{r})$, followed by the advection term, with $\boldsymbol{v}(t, \boldsymbol{r})$ the fluid velocity; the third term corresponds to radiative losses, where $P(t, E, \boldsymbol{r})$ is the energy-loss rate for a particle with energy E. Finally, $Q(t, E, \boldsymbol{r})$ is the injection function, i.e., number of injected particles/unit energy $\times$ unit volume $\times$ unit time.

We solve Equation (3) in a 3D grid $\equiv (E, r, z)$ using our own modular code (see del Valle et al. 2015, 2018). In what follows we describe each of the terms and the model details.

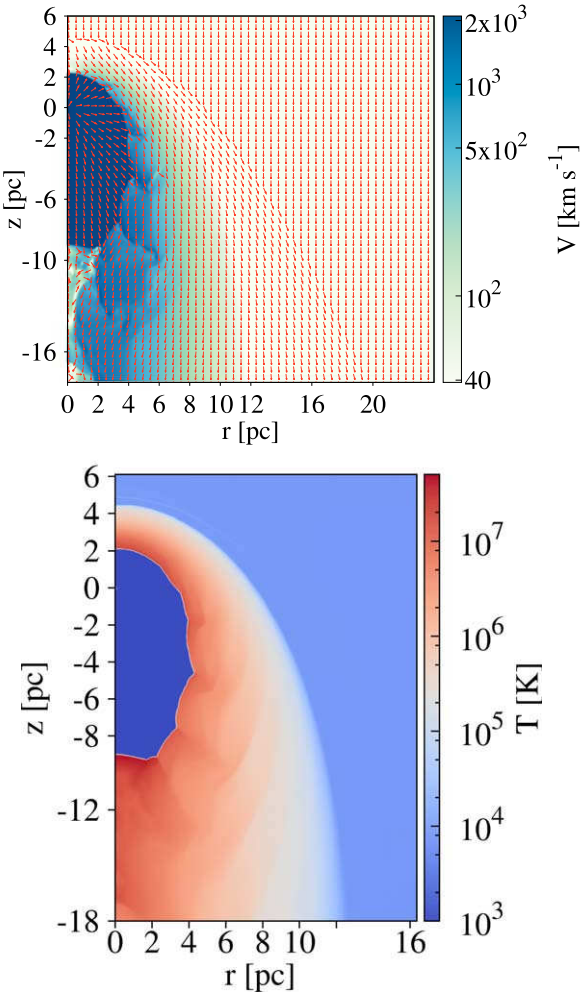

Figure 3. Top: velocity map at $t = 1.5$ Myr; the colors indicate the value of the velocity module, $\sqrt{v_r^2 + v_z^2}$, and the arrows indicate the direction of the velocity vector $\boldsymbol{v}$ in each point. Bottom: temperature map in the simulation plane, at $t = 1.5$ Myr.

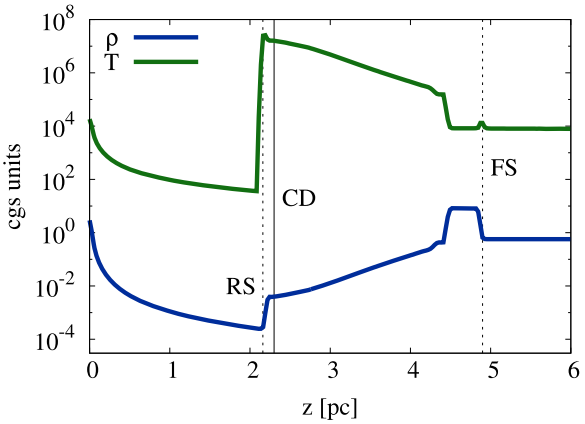

Figure 4. Density and temperature profiles for $r = 0$ as a function of z; the units are cm^{-3} and K, respectively. The reverse shock and forward shock positions are marked with dashed lines.

4.1. Injection

As argued above, the particles are thought to be accelerated in the reverse shock. Here we do not simulate directly the acceleration of the relativistic particles; instead, we assume that particles are accelerated at a rate $t_{\rm acc} = \eta r_{\rm L}/c$ (e.g., Gaisser 1990). Here $r_{\rm L}$ is the Larmor radius of a particle of energy E, i.e., $r_{\rm L} = E/e\,B$, and B is the magnetic field in the acceleration region. η is a phenomenological parameter related to the efficiency of the acceleration process, which can be approximated by $\eta \sim 20/3(c/V_{\rm shock})^2$ (Drury 1983), for a nonrelativistic diffusive shock acceleration, in a plane shock in the test-particle approximation.

We inject continuously a population of relativistic ($E > mc^2$) electrons and protons at the reverse shock position ($r_{\rm rs}$, $z_{\rm rs}$) (see below). This shock is strong everywhere; however, the density in the regions of positive z is greater than in the negative region (this is simply because these points are farther away from the star), while the wind velocity remains constant. We expect more particles to be injected in the denser regions; hence, the injection function scales as $\propto\rho(r, z)$. The particles have a power-law distribution in energy of index $\alpha = 2$, as expected from a DSA mechanism. Then the injection function reads

$$Q(t, E, r, z) = Q_0\, E^{-\alpha}\, \rho(r, z)/\rho_0\, \delta^2(\boldsymbol{r} - \boldsymbol{r}_{\rm rs}). \quad (4)$$

ρ_0 is a reference density value considered at the apsis of the wind shock; Q_0 is a normalization factor that depends on the power available in the system for particle acceleration.

The source power for accelerating the particles is the kinetic power of the wind $L_{\rm w} = 0.5\dot{M}V_{\rm w}^2$. A fraction ξ of this kinetic power is transferred to the particles in the acceleration process. Then the power in relativistic particles is $L_{\rm rel} = \xi L_{\rm w}$. We use a rather modest value of $\xi = 0.05$; for the system considered here $L_{\rm rel} \sim 4.4\times10^{34}$ erg s^{-1}. The proton-to-electron flux ratio a, for an acceleration process that leads to a power law in momentum (the same for electrons and protons), is calculated in Pohl (1993). In later work the authors assumed that the same number rate of electrons and protons is accelerated from the same initial energy for both species. For a power-law index $\alpha \neq 2$, $a = (m_p/m_e)^{(3-\alpha)/2}$. In the case in which $\alpha = 2$, a depends very weakly on the particles' maximum energies and is of the order of $\sim$40. Starting from $a \sim 40$, the value of $a = 100$ observed in cosmic rays can be easily explained from propagation effects. In this work we assume $a = 40$, and in Section 6 we discuss the implications of adopting others values for ξ and a.

For obtaining the position ($r_{\rm rs}$, $z_{\rm rs}$) of the reverse shock we search for a jump in the temperature function $T(r, z)$ (shown in the bottom panel of Figure 3), in the wind material.

4.2. Diffusion

Stellar winds are very turbulent systems, in particular the system we are studying, in which the wind collides with the incoming ISM (see Section 3). In such a scenario slow particle diffusion is expected, as in the case of the Sun, where a particle of $E \sim 100$ MeV in the solar wind has a mean free path of $\lambda \sim 1$ au, which gives a diffusion coefficient $D \approx 10^{23}$ erg s^{-1}.

We assume the diffusion coefficient to depend only on the particle energy, i.e., $D(t, E, \boldsymbol{r}) \equiv D(E)$. Close to the shock the diffusion is in the Bohm regime; at a certain scale a transition occurs from this slow Bohm diffusion to the fast diffusion estimated in the Galaxy (e.g., Telezhinsky et al. 2012). The characteristic scale of the system we are studying here, given by Equation (1), is of the order of parsecs, hence the more

convenient assumption of a *Galactic-like* diffusion coefficient:

$$D(E) = D_{10\,\mathrm{GeV}}\left(\frac{E}{10\,\mathrm{GeV}}\right)^{\delta}\ \mathrm{cm^2\,s^{-1}}. \quad (5)$$

Here $D_{10\,\mathrm{GeV}}$ is the value of the diffusion coefficient at $E = 10$ GeV, and δ is a power-law index varying in the interval 0.3 and 0.6, depending on the power-law spectrum of the turbulence of the magnetic field. Typical values for the Galaxy are $D_{10\,\mathrm{GeV}} = 10^{28}\ \mathrm{cm^2\,s^{-1}}$ and $\delta = 0.5$ (e.g., Berezinskii et al. 1990). As discussed above, in this system values much lower than this are expected owing to the presence of turbulence.

In this work we use $\delta = 0.5$ and two values for $D_{10\,\mathrm{GeV}}$: $10^{25}\,\mathrm{cm^2\,s^{-1}}$ for the slow case, and $10^{27}\,\mathrm{cm^2\,s^{-1}}$ for a fast diffusion situation. We can estimate a characteristic timescale for diffusion t_{diff} considering the typical spatial scale of the problem R_0; this is also approximately the minimum distance between the injection position and the bow shock itself (the dense cooled ambient matter),

$$t_{\mathrm{diff}} \sim \frac{R_0^2}{D_{10\,\mathrm{GeV}}}. \quad (6)$$

Then, $t_{\mathrm{diff}} \sim 1.5$ and 150 kyr for fast and slow diffusion, respectively (see Section 4.6).

4.3. Advection

The velocity field responsible for the advection of particles is shown in the top panel of Figure 3. As the system is in steady state, $\boldsymbol{v}$ does not depend on time. We can distinguish here between wind advection and ISM advection.

We can estimate a characteristic timescale t_{adv}, as done above for the diffusion, for the wind:

$$t_{\mathrm{adv,w}} \sim \frac{R_0}{v}. \quad (7)$$

The velocity is $v \leqslant 2 \times 10^3\ \mathrm{km\,s^{-1}}$, and then $t_{\mathrm{adv,w}} \geqslant 1$ kyr.

The vertical advection produced by the ISM is relevant almost everywhere, for $v = 40\,\mathrm{km\,s^{-1}}$, and then $t_{\mathrm{adv,ISM}} \sim 54$ kyr. It is clear that advection dominates the transport in the case of slow diffusion. A particle injected at $z \sim -9$ pc would reach the bottom boundary in ∼200 kyr. In that time, for the slow regime, a 10 GeV particle would radially diffuse approximately 2.7 pc before it reaches the bottom boundary, and a TeV particle 8.5 pc.

Toward the $+z$-direction the situation is more complicated because the advection in the inner regions of the bow shock is not vertical. After being injected, the particles are advected in the shocked wind, with $v \sim v_w/4.0$. The particles reach out a distance $\approx D/v = 0.08$–0.24 pc for $E = 10$ GeV–1 TeV, respectively. In the case of fast diffusion these distances are two orders of magnitude higher.

4.4. Nonthermal Losses

The third term in Equation (3) accounts for the relevant nonthermal losses that particles suffer after their injection in the system. For electrons the nonthermal processes considered are relativistic bremsstrahlung, synchrotron, and IC scattering with the stellar and reprocessed stellar photons (dust emission). For protons the only energy losses considered are due to $p-p$ inelastic collisions. All the target fields—magnetic, density, and radiation fields—are inhomogeneous. The density field is directly taken from the simulations; below we describe how we construct the rest of the fields.

4.4.1. Magnetic Field

We reconstruct the magnetic field from the stars's magnetic field $B_\star$, the ISM magnetic field B_{ISM}, and density compression. We assumed no preferred direction for the field, which is assumed to be randomly distributed in the entire domain. We consider four regions: the stellar wind region, the shocked wind, the shocked ISM, and the ISM itself. For the wind region we use the approach made in Voelk & Forman (1982); assuming flux conservation, they obtained a field that decreases $\propto R^{-1} = \sqrt{r^2 + z^2}$:

$$B_{\mathrm{wind}} = B_\star\left[1 + \left(\frac{V_{\mathrm{w}}}{V_{\mathrm{rot}}}\right)^2\right]^{-1/2}\left(\frac{R_\star}{R}\right)\left[1 + \left(\frac{R_\star V_{\mathrm{w}}}{R V_{\mathrm{rot}}}\right)^2\right]^{1/2}, \quad (8)$$

V_{rot} is the rotational velocity (we use a typical value of $100\,\mathrm{km\,s^{-1}}$). In the reverse shock the magnetic field is allowed to compress by a similar factor to the density. Beyond the discontinuity[4] between the wind and ambient material at the coordinates $(r_{\mathrm{dis}}, z_{\mathrm{dis}})$, the magnetic field is assumed to be that of the ISM rescaled with the density field at each point.

Hence, $B(r, z)$ reads

$$B(r,z) = \begin{cases} B_{\mathrm{wind}} & \text{if} \quad (r,z) \leqslant (r_{\mathrm{rs}}, z_{\mathrm{rs}}) \\ B(r_{\mathrm{rs}}, z_{\mathrm{rs}}) \times \mathcal{F}_1 & \text{if} \quad (r_{\mathrm{rs}}, z_{\mathrm{rs}}) \leqslant (r,z) \leqslant (r_{\mathrm{dis}}, z_{\mathrm{dis}}) \\ B_{\mathrm{ISM}} \times \mathcal{F}_2 & \text{if} \quad (r_{\mathrm{dis}}, z_{\mathrm{dis}}) \leqslant (r,z) \leqslant (r_{\mathrm{ISM}}, z_{\mathrm{ISM}}) \\ B_{\mathrm{ISM}} & \text{if} \quad (r,z) \geqslant (r_{\mathrm{ISM}}, z_{\mathrm{ISM}}) \end{cases}, \quad (9)$$

where $\mathcal{F}_{1,2} = \sqrt{2(\mathcal{K}_{1,2}^2 - 1)/3 + 1}$, with $\mathcal{K}_1 = \rho(r_{\mathrm{rs}}, z_{\mathrm{rs}})/\rho(r,z)$ and $\mathcal{K}_2 = \rho(r_{\mathrm{ISM}}, z_{\mathrm{ISM}})/\rho(r,z)$. The factors $\mathcal{F}_{1,2}$ account for the shock compression effect in the random field; for a strong shock $\mathcal{K} = 4$ and $\mathcal{F} = \sqrt{11}$. Here we use $B_\star \sim 100$ G (Walder et al. 2012); however, we consider a greater value in Section 5. For the ambient medium we use $B_{\mathrm{ISM}} \sim 5\,\mu$G. Figure 5 shows the map of the magnetic field in the computational domain. The white curve shows the position of the reverse shock: the injection position; the gray curve shows the material discontinuity between the shocked wind and ISM.

4.4.2. Target Radiation Fields

As stated before, the target radiation fields are those from the star and from the bow shock itself. The stellar photon field is assumed to be that of a blackbody at T_{eff}, decaying as R^{-2} away from the star. For the IC emission calculations we assume the field to be monoenergetic, with $E_{\mathrm{ph}} = k_{\mathrm{B}} T_{\mathrm{eff}}$.

Computing the radiation field for the reprocessed emission is more complicated because it requires adopting a dust model. The emission of the bow shock, mainly at IR, is produced by dust heated by starlight.[5] Here we adopt a thermal

[4] The position of this discontinuity is computed using the tracer values at $t = 1.5$ Myr.

[5] The produced emission by collisionally heated dust grains is subdominant in these systems (Meyer et al. 2014).

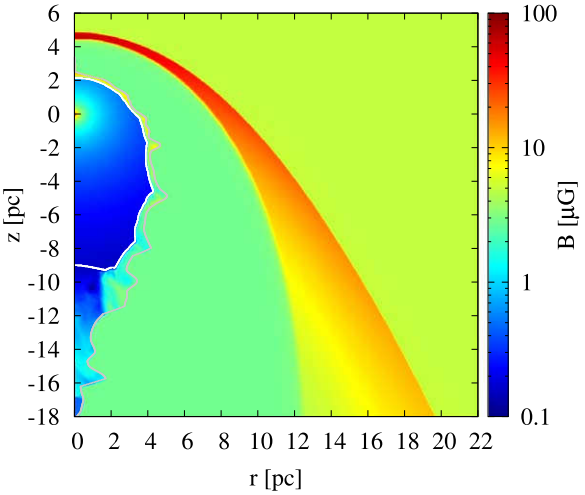

Figure 5. Magnetic field map in the computational domain, reconstructed from Equation (9), $B_{\rm ISM}$, and the density map. The white curve shows the position of the wind shock, where the particles are injected into the domain; the gray curve shows the material discontinuity.

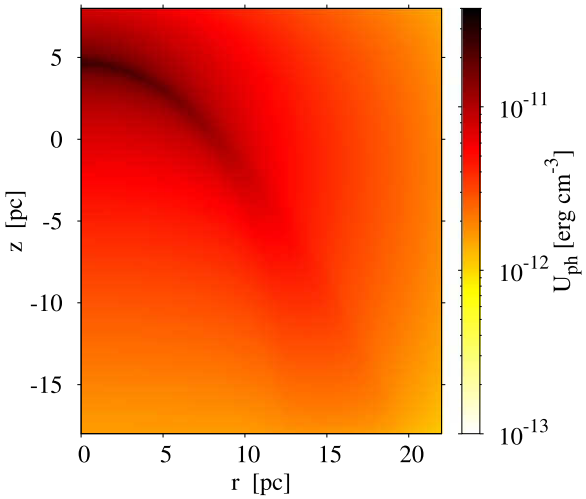

Figure 6. Infrared photon target energy density in the computational domain.

approximation for the dust emission, with grains in thermal equilibrium. This treatment is appropriate given that the observed fluxes of the bow shocks are in the mid-IR (MIR) to far-IR (FIR).

In order to calculate the equilibrium temperature $T_{\rm gr}$ of the dust grains, we equate the absorbed energy with the emitted one. In equilibrium the absorbed energy by the dust should be the same energy it radiates (Lequeux 2005; Draine 2011):

$$\int_0^\infty I_\nu \pi a^2 Q_{\rm abs}(\nu)\, d\nu = \int_0^\infty 4\pi a^2 Q_{\rm em}(\nu)\pi B_\nu(T_{\rm gr}) d\nu. \quad (10)$$

Here we use a spherical dust grain of radius a. The left-hand side is the frequency integration of the incident flux from the star, which scales with distance as R^{-2}, multiplied by the absorption efficiency and the grain cross section. The right-hand side is the integration over frequency of the surface of the grain times the emitted spectrum. The dust emissivity is a modified blackbody at $T = T_{\rm gr}$; this is $B_\nu(T_{\rm gr})$ multiplied by an emissivity function $Q_{\rm em}(\nu)$. The emissivity function is a power law in frequency; we use a standard model with $Q_{\rm em} \propto \nu^2$.

For estimating the temperature above we use the so-called Plank-averaged absorption in the ultraviolet (UV) $\langle Q_{\rm abs}\rangle$ and emission efficiencies $\langle Q_{\rm em}\rangle$ in the IR (Draine 2011). In the UV the absorption efficiency can be approximated by unity; this is valid as long as the grain sizes are of the order of the UV photon wavelengths[6] (i.e., 0.01 $\mu{\rm m} \leqslant \lambda \leqslant 0.4$ μm). The grain temperature depends on the position and is given by

$$T_{\rm gr} = \left(\frac{R_\star}{\sqrt{r^2+z^2}}\right)^{1/3} \frac{T_\star^{2/3}}{(4\pi\langle Q_0\rangle)^{1/6} a_{\mu{\rm m}}^{1/3}}. \quad (11)$$

We assume no dust in the stellar wind region. Dust grains exhibit a distribution of sizes, believed to be a power law in a. For the sake of simplicity, we consider that all grains have the same radius. The dust temperature is of the order of $T_{\rm gr} \sim 100$ K, which is consistent with bow shocks being detected in the IR at $\lambda \sim 22$ μm (e.g., Peri et al. 2012), because the maximum of the dust radiation occurs at $\lambda_{\rm max} \sim 2 \times 10^3/T_{\rm gr}$ μm.

The emissivity depends on the amount of dust, i.e., it scales with density and temperature at each point. The energy loss by IR emission for one dust grain, i.e., the power emitted, is given by $P_{\rm gr} = 4\pi \langle Q_{\rm em}\rangle_{T_{\rm gr}} \sigma T_{\rm gr}^4$ (Draine 2011) . Then for a number of grains per unit volume $n_{\rm gr}$, the total power per unit volume is $P = n_{\rm gr} P_{\rm gr}$. For computing $n_{\rm gr}$ we assume a typical gas-to-dust density ratio of 100 and estimate the mass of each dust grain as $m_{\rm gr} = 4\pi a^3 \rho_{\rm gr}$, with $\rho_{\rm gr} \sim 2$ gr cm^{-3} (Draine & Li 2007). The resulting expression is (all units are in cgs)

$$P(r,z) = \chi \frac{3}{200} \langle Q_0\rangle\, \sigma T_{\rm gr}^6(r,z)\, \rho(r,z)\ {\rm erg\ s^{-1}\ cm^{-3}}. \quad (12)$$

Here χ is a factor such that the luminosity from dust in the region does not exceed the star luminosity, i.e., $4\pi\sigma T_\star^4 R_\star^2$.

For obtaining the energy density of the photon field in each point we compute $U_{\rm ph}(r,z) = \int P/(4\pi\, c\, d^2) dV$, with $d \equiv d(x,y,z)$ the distance of each point to the emitting source and P given by Equation (12). The energy density maps of the target IR photon field are shown in Figure 6 for grain size $a_{\mu{\rm m}} = 0.01$. Even though P does not depend explicitly on the size of the grain, it depends strongly on the dust temperature. In a real source the grains responsible for the IR radiation have a size distribution; however, the grain size distribution is a power law with index smaller than -3, and then it is more probable to encounter smaller dust grains. Note that the grains responsible for the stellar photons' absorption cannot be smaller than $a_{\mu{\rm m}} = 0.01$. The IR photon field in the IC calculations is also assumed as monoenergetic, with $E_{\rm ph} = k_{\rm B}\langle T_{\rm gr}\rangle$, where $\langle T_{\rm gr}\rangle$ is the mean grain temperature in the computational region.

4.5. Maximum Particle Energies

The maximum energy that particles achieve in a DSA process depends on many factors. Its estimation is not straightforward given that the mechanism is nonlinear. However, we can make an order-of-magnitude estimation by comparing the gain rate per energy with the losses in the acceleration region (only in the case of electrons; in the case of protons their energy losses are not limiting their acceleration) or by the limit imposed by the size of the acceleration region (a constraint valid for both electrons and protons).

[6] This is the case for the relatively large dust grains responsible for the IR radiation detected in massive runaway stars' bow shocks.

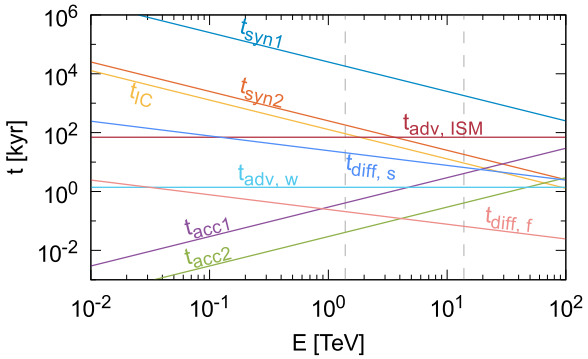

Figure 7. Timescales involved in the physical processes of the system as a function of the electron energy. The plotted scales are the synchrotron cooling time for two values of the stellar magnetic field, the cooling time for the IC scattering with dust photons for $U = 10^{-11}$ erg cm^{-3}, the acceleration time for two values of the stellar magnetic field, the diffusion time for the slow and fast cases, and the advection time for the wind and the ISM. The vertical dashed lines show the maximum energies imposed by the system size for two values of the stellar magnetic field. See the text for further details.

For estimating $E_{\rm max}$ from the losses we equate $t_{\rm acc} = \min(t_{\rm synchr}(r_{\rm rs}, z_{\rm rs}); t_{\rm IC}(r_{\rm rs}, z_{\rm rs}))$. Given the physical size of the system (see Figures 2 and 4), the acceleration process then should proceed in a region of size of order of $l \sim 1$ pc. Imposing the condition that the precursor size should be smaller than 1 pc and assuming Bohm diffusion for the acceleration, we obtain the maximum energy, i.e., $E < 3\, e\, B|_{\rm shock}\, V_{\rm shock}\, l/c$; we use 10% of this value. Both methods for obtaining the maximum energy are sensitive to the magnetic field and the shock velocity.

For the system analyzed here the size of the acceleration region constrains the maximum energies, giving $E_{\rm max} \sim 1.3$ TeV for electrons and protons, with $B|_{\rm shock} \sim 0.7\ \mu$ G. Note that these values are different when other values for the magnetic field are considered (see Section 5.2).

4.6. Timescales

The timescales discussed so far are plotted in Figure 7, as a function of the electron energy. The synchrotron losses are shown for two values of the magnetic field strength, $B|_{\rm shock} = 0.7$ and $B|_{\rm shock} = 7\ \mu$G, with the subindices 1 and 2, respectively (see Section 5.2). This corresponds to two stellar magnetic field values $B_\star = 10^2$ and 10^3 G. The acceleration time is also plotted for the two $B|_{\rm shock}$ values. The IC losses[7] due to dust photon scattering are plotted for a representative constant value of U of 10^{-11} erg cm^{-3} (see Figure 6).

The timescales for the transport processes are also presented in Figure 7. For the diffusion we plot the timescale for the two cases studied here: fast and slow. We show the cases of advection produced by the wind and by the ISM. The dashed vertical lines indicate the maximum energy arising from the constraint imposed by the size of the system, for the two values of $B|_{\rm shock}$ considered (see Section 4.5).

From the figure we can conclude that transport effects are of great significance and dominate over the losses, at least at the injection position. Fast diffusion dominates the transport for energies greater than 50 GeV. In the case of slow diffusion it dominates the transport over the ISM advection for energies greater than 0.2 TeV and the wind advection for very high energies (i.e., $E > 265$ TeV).

[7] We consider here only the Thomson regime, which is appropriate for the energies of interest.

4.7. Calculation Details

Equation (3) is solved using a discrete grid $(E, r, z) \in [1\ {\rm keV}, 10\ {\rm TeV}] \times [0, 24\ {\rm pc}] \times [-12, 10\ {\rm pc}]$, using the finite-volumes method. The energy grid is logarithmically spaced, and the spatial grid is uniform. The used grid resolution for (E, r, z) is $(L, M, K) = (128, 128, 128)$, respectively. Particles are injected through all of the integration time. The resulting $N(t, E, r, z)$ for electrons and protons are interpolated into a 3D spatial grid. We calculate the nonthermal radiation produced by the particles as they diffuse through the domain. The integration proceeds until there are no significant changes in the radiation outcome.

Initially we assume $N(0, E, r, z) \equiv 0$, i.e., no particles inside the domain. The energy boundary conditions are $N(t, E > E_{\rm max}, r, z) = 0$ and $N(t, E < E_{\rm min}, r, z) = 0$. This does not influence the system evolution, because the upper limit is above the maximum energy of the injected particles, and the advection in the energy space is always directed to smaller energies. The outer boundary condition for r and the inner and outer boundary conditions for z are assumed as outflow; also no inflow is allowed at the inner z boundary. We adopted axial symmetry at the r inner boundary.

The numerical integration is performed through the operator splitting method. Each time-step integration computes the evolution of the particle density distribution on the grid through four substeps: first the losses are integrated, then the spatial advection, followed by spatial diffusion, and finally the source term is added. The time steps were chosen in accordance with the CFL stability criterion. Further description of the code is made in del Valle et al. (2015, 2018).

5. Results

In Figure 8 we show a map of the distribution of electrons for $E = 10$ GeV, for different evolution times. The 2D maps are constructed integrating the 3D data along an arbitrary line of sight, chosen here to be on the y-direction. This plot corresponds to the slow diffusion case $D_{10\ {\rm GeV}} = 10^{25}$ cm^2 s^{-1}. The integration time or injection time $t_{\rm inj}$ is taken as 230 kyr. This time is enough for a particle injected at $z \sim -9$ pc to cross the bottom boundary. From the maps it can be seen that particles are injected in the reverse shock position and then advected and diffused in the plane. The maximum number of electrons is always near the injection region, and when $t = 230$ kyr, all of the domain is reached by particles. Only a few particles, the most energetic ones, reach the wind region, and most of them are advected away by the wind. There are some bright spots in which particles are accumulated, because the velocity is very low in these regions and diffusion is slow (see Figure 3). In the top panel of Figure 9 we show the IC map for $E = 10$ GeV at the final time $t = 230$ kyr. The maximum emission occurs in the vicinity of the reverse shock. It becomes stronger in the region above the injection position as the electrons reach by diffusion the regions of highest $U_{\rm ph}$ (see Figure 6), slightly tracing the bow shock structure. This last effect is stronger for the synchrotron emission, whose map at $E \equiv 1.4$ GHz is shown in the bottom panel of Figure 9. The behavior exhibited by this emission is similar: the maximum

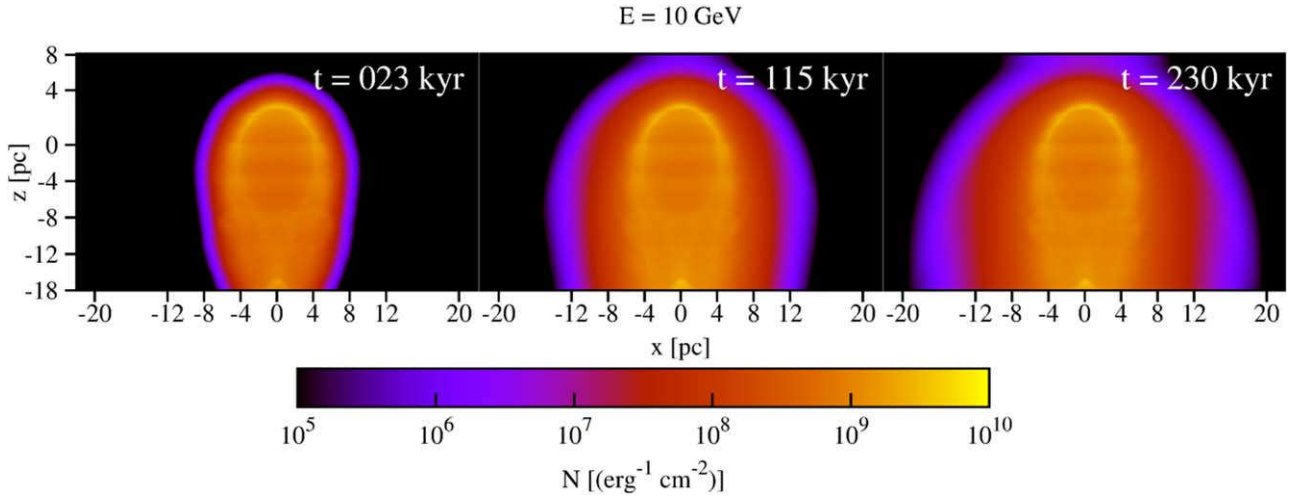

Figure 8. Electron distribution at fixed energy projected along the line of sight for the slow diffusion case; $E_e = 10$ GeV. Time evolves from left to right.

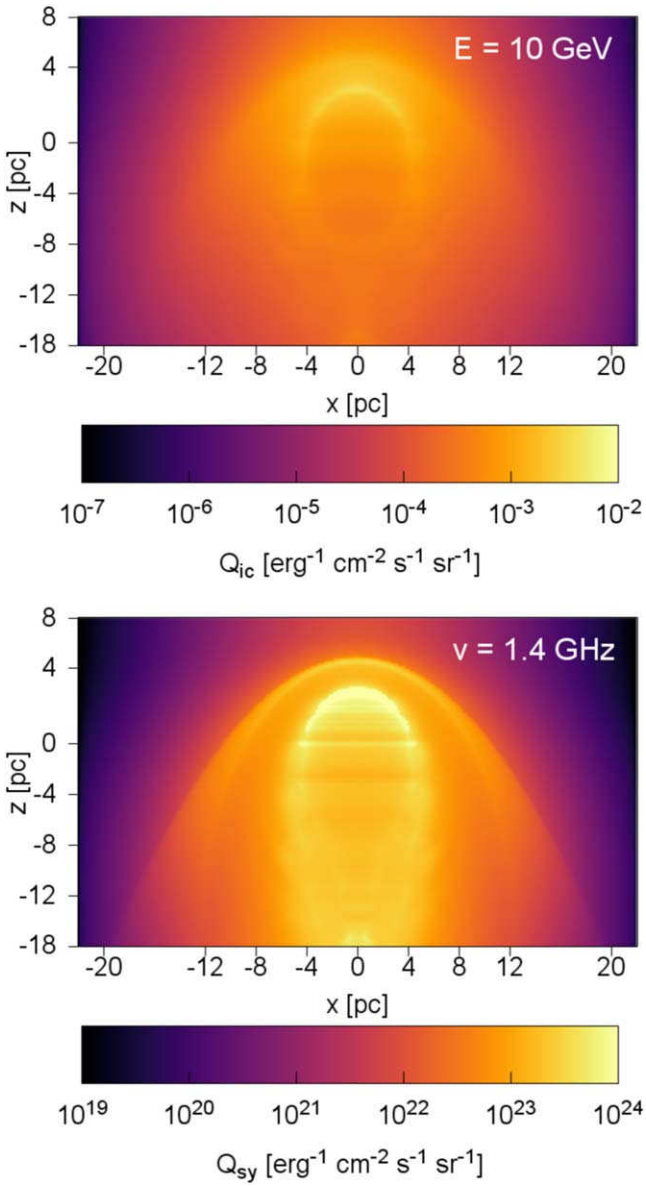

Figure 9. Intensity evolution, projected along the line of sight for IC at $E = 10$ GeV (top) and synchrotron at $E \equiv 1.4$ GHz (bottom); the figures correspond to $t = 230$ kyr.

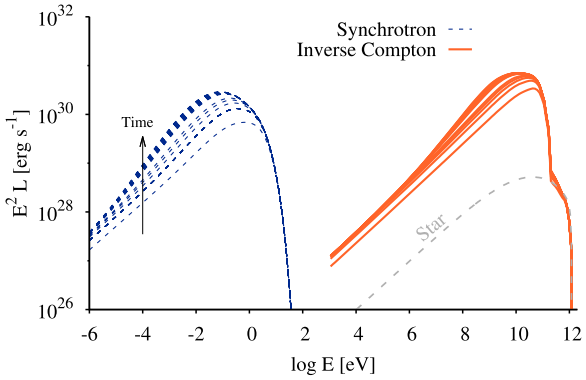

Figure 10. SED for different integration times from the bow shock of a massive runaway star. The gray curve illustrates the contribution to the IC of the stellar photons. The black arrow indicates that the radiation grows with time.

here occurs in the shocked wind region and then in the shocked ISM.

The volume integration of the nonthermal luminosity—the SED—for the slow diffusion case is shown in Figure 10. Only the dominant processes are shown: IC scattering and synchrotron. The luminosity grows with time, as indicated with the black arrow in the plot. However, after some time, the emission stops growing. This is because a steady state is reached between the injection, advection, losses, and diffusion of particles in the domain. This can be appreciated in the pileup of the curves in the SED as time passes. The two IC components, from the star and from the dust emission, can be distinguished in the curves. For illustration we have plotted the contribution from the stellar photons in gray. As can be seen in Figure 10, this component is rather weak.

The emission from interactions with matter (relativistic bremsstrahlung and p–p inelastic collisions) is very low when compared with IC, with maximum luminosities $\sim 10^{30}$ erg s^{-1}; hence, the hadronic contribution to the emission is unimportant, and the relativistic protons diffuse out of the system almost without energy loss as predicted previously (del Valle et al. 2015). We are not discussing these emission components any further.

The spectrum of the resulting SED depends, among other factors, on the shape of the injected particles. A change on the

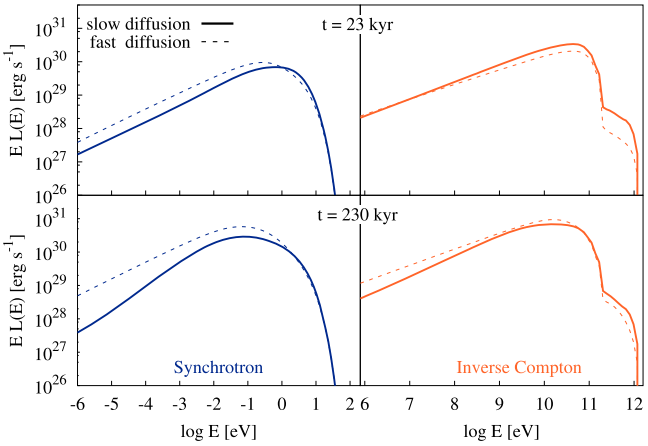

Figure 11. SEDs, at different integration times, for different diffusion regimes: slow ($D_{10\,\mathrm{GeV}} = 10^{25}$ cm^2 s^{-1}) and fast ($D_{10\,\mathrm{GeV}} = 10^{27}$ cm^2 s^{-1}).

spectral index will alter the photon distribution. In a DSA process at a nonrelativistic shock we expect $\alpha \sim 2$, but the spectral index can deviate from that value (see, e.g., Longair 2011). In the case of an injection $\alpha = 1.8$ the emission through all of the spectrum diminishes by a factor of ∼2.2 owing to a change in the particle normalization ($a \sim 90$; see Section 4.1). Also, the distribution of radiation in the SED changes, and more emission is produced at the highest energies; on the contrary, the radiation diminishes at radio and X-rays. At the highest energies the shape of the SED is modified by diffusion, and its shape is influenced by the dependence of the diffusion coefficient on energy.

The gamma emission coming from $z > 0$ (the apsis of the bow shock) dominates the radiation output. For example, for $E = 100$ GeV the IC intensity at $z = 8$ pc is twice that at $z = 26$ pc, meaning that the radiation density is higher in this region and the bulk of the emission is coming from here. This is because the IR target radiation field is strong and the injection is higher in this region.

5.1. Dependence on Diffusion

We consider slow ($D_{10\,\mathrm{GeV}} = 10^{25}$ cm^2 s^{-1}) and fast ($D_{10\,\mathrm{GeV}} = 10^{27}$ cm^2 s^{-1}) diffusion to study how these different regimes affect the nonthermal luminosity. In Figure 11 we show the dominant nonthermal components at $t = 23$ kyr (top panel) and at $t = 230$ kyr (bottom panel). Initially the differences between the cases are not so important, but in the IC star component, which is stronger in the case of slow diffusion, the particles stay for a longer time in the vicinity of the injection region, where the stellar radiation field is stronger. The fast diffusion slightly dominates the synchrotron component for $E < 1$ eV; this is because the high-energy particles reach regions of stronger magnetic field (see Figure 5). At the final integration time the fast diffusion dominates the SED, except for the IC star component; this is because particles in the slow diffusion are dragged by advection and very few reach the regions of highest magnetic and IR photon field; as discussed in Section 4.3, in the slow diffusion case, due to advection, a typical particle will not reach the denser bow shock.

5.2. Dependence on Magnetic Field

Here we assume a greater value for the stellar magnetic field, with $B_\star = 1$ kG. This might affect the magnetic field in the wind region, and it might change the hydrodynamics of the system, changing, among other things, the reverse shock position. If the magnetic pressure is of the same order as or higher than the wind ram pressure, the pressure balance (see Section 2) between the wind and the ISM occurs at greater distances from the star. The relevance of the effects of the magnetic field on the hydrodynamics can be estimated by comparing the ram pressure $\rho_\mathrm{w} V_\mathrm{w}^2$ with the magnetic pressure of the wind $B_\mathrm{wind}^2/8\pi$. The wind ram pressure is given by

$$P_\mathrm{r,w} = \frac{\dot{M}_\mathrm{w}}{4\pi R^2 V_\mathrm{w}} V_\mathrm{w}^2 \equiv \frac{p_\mathrm{r\,w}}{R^2}; \tag{13}$$

the last factor of Equation (8) tends to 1 very fast for $R > 20\,R_\star$, and then the magnetic pressure is

$$P_\mathrm{B,w} = \frac{B_\star^2}{8\pi}\left[1 + \left(\frac{V_\mathrm{w}}{V_\mathrm{rot}}\right)^2\right]^{-1}\left(\frac{R_\mathrm{star}}{R}\right)^2 \equiv \frac{p_\mathrm{B\,w}}{R^2}. \tag{14}$$

Then, the pressure ratio $P_\mathrm{r,w}/P_\mathrm{B,w} \sim 7$ for this case, and the magnetic field in the wind is not expected to affect dramatically the hydrodynamics and can be ignored at least at first order.

The magnetic field at the reverse shock $B|_\mathrm{shock}$ grows by one order of magnitude; hence, t_acc increases and electrons reach a higher maximum energy in the acceleration process (see Section 4). In this case we obtain E^e_max, $E^p_\mathrm{max} \sim 13.8$ TeV.

No great differences in the IC radiation occur, except the ones expected from the change in E^e_max, which is 10 times higher than in the reference case. The gamma spectrum is shifted toward higher energies, increasing the total emission output (see Section 6). Naturally, the synchrotron emission is much higher; it dominates the SED in X-rays until $E \sim 6.3$ keV, with $L_\mathrm{syn} \sim 8 \times 10^{29}$ erg s^{-1} at $E \sim 1$ keV and $L_\mathrm{syn} \sim 2 \times 10^{27}$ erg s^{-1} at $E \sim 6.3$ keV.

5.3. Dependence on the Stellar Velocity

The bow shock size and shape of the same type of star change with $v_\star$ (see, e.g., Meyer et al. 2014). In order to study the impact of this in the nonthermal emission, we consider here the same massive star described in Section 3, but with a higher velocity: $v_\star = 70$ km s^{-1}. For this system the global steady state is reached at ∼4 Myr. For numerical stability here we use a Harten–Lax–van Leer solver. As can be deduced from the expression of R_0 (see Equation (1)), the whole bow shock structure is smaller.

The injection region is closer to the star; hence, the magnetic field near the injection region has greater values. The maximum energy particles might achieve is slightly higher than the previous case, with $E^e_\mathrm{max} \sim 2$ TeV. We compute the SED for slow diffusion. The synchrotron emission reaches higher energies than in the reference case, as a combination of a greater magnetic field near the injection region and a slightly higher electron maximum energy. Both the synchrotron and IC emission are higher in this case, by a maximum factor of 4 at the same energies. This is because the maximum values of the target fields are closer to the injection region, and hence particles lose energy more efficiently (see further discussion in Section 6).

5.4. Synchrotron Emission from the Tail

The bow shock tail can extend for several parsecs toward the $-z$-direction. The escaping electrons would produce further synchrotron emission when interacting with the magnetic field of the shocked material in the bow shock tail. In order to evaluate how important is the emission produced further downstream, we compute the emission coming from the bottom region, $-18\ \mathrm{pc} < z < -17\ \mathrm{pc}$, as an upper limit (further down the number of particles would be more diluted owing to diffusion, and the emission per pc would be lower).

The luminosity in this bottom region is a fraction 3×10^{-2} of the total one for both fast and slow diffusion; in particular at 1.4 GHz, the frequency of large-area radio surveys such as FIRST (Becker et al. 1995) and NVSS (Condon et al. 1998), the luminosity is some factor of $10^{27}\,\mathrm{erg\,s^{-1}}$ for the first case and $10^{26}\,\mathrm{erg\,s^{-1}}$ for the other. For the fast case this value is of the order of the radio detection limits of 1–2.5 mJy, which is, for a source located at 1 kpc, $(1\text{–}2.5) \times 10^{27}\ \mathrm{erg\,s^{-1}}$. For the case of fast diffusion the synchrotron emission from the tail might be important and detectable for sources at these distances or less; however, it would not be higher than the emission coming from the bow shock region. A proper calculation of this contribution is beyond the scope of this work and will be studied elsewhere.

6. Discussion

The gamma-ray photons produced in the system can be absorbed by lower-energy photons through photon–photon annihilation. The low-energy photon field can be in the source itself or in the propagation path of the gamma ray on its way to the observer. For a Galactic source this last component is negligible, and we focus on photon fields within the bow shock. For the process to occur the energies of the involved photons must fulfill[8]

$$E_\gamma \epsilon > 2(m_e c^2)^2, \tag{15}$$

where E_γ is the energy of the gamma ray and ϵ the energy of the target photon. For $E_\gamma = 100\,\mathrm{GeV}$, using $\epsilon \sim 3/2 k_\mathrm{B} T$, $T > 40{,}475$ K. This means that the stellar photon field can absorb gamma-rays above 100 GeV. This is not surprising; a massive star photon field is known to be a significant source of gamma-ray annihilation, for example, in a high-mass microquasar (e.g., Romero et al. 2010) or colliding-wind binaries (e.g., Bednarek & Pabich 2011). The total absorption depends strongly on the geometry and on the relative positions of the gamma ray, the stellar photon field, and the observer. However, we can make order-of-magnitude estimates. The optical depth for a gamma ray traversing a distance d is $\tau_{\gamma-\gamma} \sim \sigma_{\gamma-\gamma} n_\star d$. Here $n_\star$ is the number of photons per unit volume, which decreases quadratically with distance. The gamma-gamma cross-section maximum is $\sim\sigma_\mathrm{T}/5$, with σ_T the Thomson cross section, and it occurs close to the threshold energy. We can estimate the maximum d such that $\tau_{\gamma-\gamma} \gtrsim 1$:

$$\tau_{\gamma-\gamma} \sim \frac{\sigma_\mathrm{T}}{5} \frac{\sigma T_\star^4 R_\star^2}{\epsilon\ c\ d^2} d\ \gtrsim 1. \tag{16}$$

The last condition gives $d \lesssim 10^{-4}$ lt-yr ($\equiv 68\,R_\star$). Comparing this distance with the typical scale of the system, we get $d/R_0 \sim 10^{-5}$. Even in the least favorable case the region in which the gamma-gamma absorption is important is extremely small compared to the size of the bow shock. Then, given the large extension of the gamma-ray source, the absorption produced by the stellar photon field is negligible.

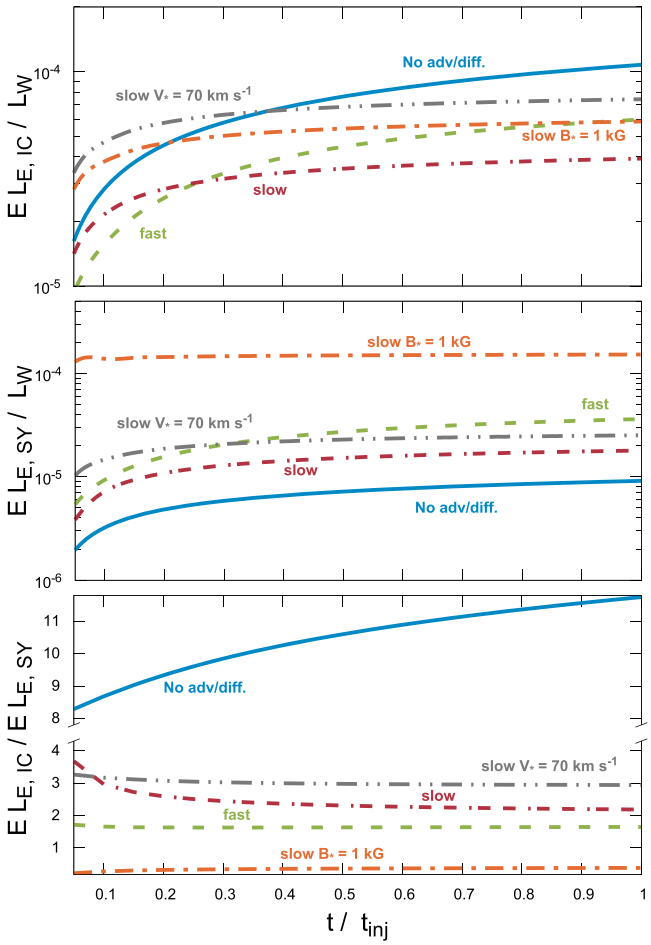

Figure 12. Evolution of the ratio of the total power produced by IC scattering (top) and synchrotron radiation (middle) to the wind's power L_w. The bottom panel shows the evolution of the IC–synchrotron power ratio.

The interaction of the stellar wind with the ISM deposits a fraction of the wind power into the ambient medium in different forms of energy. It is interesting to see then how much of the wind's power is converted into nonthermal emission as high-energy emission through IC scattering and low-energy radiation via synchrotron. This fraction as a function of the computational time is presented in Figure 12 (this depends on the assumptions made in L_rel; see Section 4.1). In this figure we show the ratio of the IC emission between 1 keV and E^e_max (top panel) to the wind's power χ_IC, for the models we consider in this work; we also show a case without diffusion or advection just for comparison. The most efficient case is that with no transport of particles, with $\chi_\mathrm{IC} \sim 10^{-4}$ (blue line) at the final time; this is expected because particles stay in the box, only losing energy by radiative losses. This is followed by the case of the star with a higher spatial velocity with a power ratio of 7.4×10^{-5} (gray line). Next comes the case with $B_\star = 1$ kG (orange line) with 5.8×10^{-5}, and the case of fast diffusion (green line) lies slightly below. Finally is the slow diffusion case (red line), which gives $\chi_\mathrm{IC} \sim 4 \times 10^{-5}$, only 3 times less than the best case. We can see that propagation effects are

[8] We assume here head-on collisions.

important. Initially all the cases show differences in χ_{IC}, but as time evolves, all cases reach values $\sim 5 \times 10^{-5}$.

In the middle panel of Figure 12 we show the ratio of the synchrotron radiation integrated between 10^{-6} and 10^{5} eV to the wind's power, χ_S. The most efficient cases do not coincide with those of the IC discussed above. The synchrotron emission is very sensitive to the magnetic field value, and in this highly spatially changing environment the propagation effects are really important. This can be noticed when analyzing the case of no diffusion and no advection: the efficiency is the lowest with a ratio to the wind's power of 9×10^{-6}. Small differences are exhibited at the final times in the case of slow and fast diffusion, with 2×10^{-5} for the slow case and 4×10^{-5} for the fast case; once the particles reach by diffusion the regions of higher magnetic field, they radiate more effectively. When the particles are injected in a region where the magnetic field is higher, the particles radiate more power, as in the case of a smaller bow shock (gray curve), for which χ_S is 2.5×10^{-5}. The extreme case with a higher stellar magnetic field is very efficient, with $\chi_S \sim 10^{-4}$. Again, for the final time there are no big differences in the energy injected as synchrotron radiation, which is $\chi_S \sim 3 \times 10^{-5}$.

From the value of χ_{IC} we can also estimate what fraction of the injected power is radiated in the IC process: $L_{IC}/L_{rel} \sim \chi_{IC}/\xi \sim 8 \times 10^{-4}$ to 2×10^{-3}. For the synchrotron we get a slightly smaller number (see next paragraph). We can see that electron radiation is not efficient and the electrons are transported out of the system by diffusion and advection before they can lose a significant fraction of their power, in accordance with the timescale estimations presented in Figure 7.

We analyze also the evolution of the power ratio between the two dominant radiation mechanisms. This ratio is shown in the bottom panel of Figure 12 for all the configurations studied here. The synchrotron power only dominates in the case of a higher stellar magnetic field by almost one order of magnitude. In general, the ratio between the emitted powers is of order unity, dominated by IC, with the exception of the case with no transport effects. In this case the IC power is one order of magnitude greater than the synchrotron power, again consistent with the timescales shown in Figure 7.

From the above analysis we can infer very generally the following:

$$L_{IC} \lesssim 10^{32}\left(\frac{\dot{M}}{10^{-6} M_\odot \ \mathrm{yr}^{-1}}\right)\left(\frac{V_w}{2000 \ \mathrm{km \ s}^{-1}}\right)^2 \times \left(\frac{\chi_{IC}}{10^{-4}}\right)\left(\frac{40}{a}\right)\left(\frac{\xi}{0.05}\right)\mathrm{erg \ s}^{-1},$$

$$L_{Sy} \lesssim 5 \times 10^{31}\left(\frac{\dot{M}}{10^{-6} M_\odot \ \mathrm{yr}^{-1}}\right)\left(\frac{V_w}{2000 \ \mathrm{km \ s}^{-1}}\right)^2 \times \left(\frac{\chi_S}{5 \times 10^{-5}}\right)\left(\frac{40}{a}\right)\left(\frac{\xi}{0.05}\right)\mathrm{erg \ s}^{-1}. \quad (17)$$

We explicitly show the dependence with the shock efficiency ξ and proton-to-electron power ratio a. In the case of IC the maximum power is around $\sim$100 GeV with a luminosity of approximately 10% of the above value. These are modest values for a gamma-ray source. For the synchrotron, the maximum luminosity lies around $\sim$1 eV, ignoring the extreme case with $B_\star = 1$ kG. The value of a changes in two cases. If the injection index changes (this was discussed previously), in the case of a softer index ($\alpha > 2$) a decreases, and it increases for harder indices ($\alpha < 2$). The other case is that if the condition for equal injected number rate for both species is relaxed, smaller values can occur if more electrons are injected. The shock efficiency ξ adopted here is modest; it can be higher, between 10% and 20%, as obtained in numerical simulations (Caprioli & Spitkovsky 2014) or observations of Earth's bow shock (Ellison et al. 1990).

We can apply Equation (17) to the case of Lambda Cep associated with a *Fermi* source (Sánchez-Ayaso et al. 2018). For $\dot{M} \sim 7 \times 10^{-6} M_\odot$ yr^{-1} and $V_w \sim 2200$ km s^{-1} (Mokiem et al. 2007), we get $L_{IC} \lesssim 8.5 \times 10^{32}\left(\frac{40}{a}\right)\left(\frac{\xi}{0.05}\right)$erg s^{-1}. This result is consistent with the gamma source power at 100 GeV of $\sim 10^{32}$ erg s^{-1}. The case of LS 2355 is more complex because the system is interacting with an H II region.

According to our model, the maximum emission from massive runaway bow shocks is not to occur in the very high energy domain, i.e., >TeV. Our results from Figure 12 are in agreement with H.E.S.S. upper limits, i.e., $L_{IC}[0.14\text{–}18 \ \mathrm{TeV}] < 10^{-2} \ L_W$ (H.E.S.S. Collaboration et al. 2018). Concerning the upper limits from *Fermi* from Schulz et al. (2014), although they are for specific sources, for those investigated in De Becker et al. (2017) with distances ranging between 200 and 2000 pc, these upper limits range between 10^{33} and 10^{35} erg s^{-1} in the four energy bands. Not even our most favorable model at gamma-rays reaches these upper limits; however, for the case of a more powerful wind it might reach these levels (see Equation (17)). In general, the distances of the bow shocks cataloged in the E-BOSS (Peri et al. 2012) also ranged between $\sim$200 and 2000 pc; the theoretical 5σ sensitivity of *Fermi* in the energy range between 1 and 10 GeV is $\sim 10^{-11}$ erg s^{-1} cm^{-2} (it can be smaller for sources above the plane). For sources at 200 and 2000 pc the threshold luminosity is $\sim 5 \times 10^{31}$ and 5×10^{33} erg s^{-1}, respectively. These values are not unrealistic for our model. However, a note of caution is in order: the power in relativistic electrons might be superestimated, as can be learned from the radio upper limits as discussed below.

The 3σ radio upper limits in the case of the sources from the study of De Becker et al. (2017) are more restrictive than those at gamma-rays. These upper limits are obtained from the NRAO VLA Sky Survey (NVSS), a 1.4 GHz ($\sim 5.8 \times 10^{-6}$ eV) continuum survey. These values range between 10^{27} and 10^{28} erg s^{-1}. If these limits are applied to a system like the one we are studying here, then the synchrotron power we obtain with our models is roughly over these limits. This means that in the presence of a relatively high magnetic field the power in electrons assumed here could be overestimated by at least the same factor. If this is the case, then the IC luminosity is lower than the one predicted in our models. Another possibility is that the magnetic field is overestimated.

Very low values of the magnetic field are not good either for producing higher values of gamma emission. Particles need magnetic field to be efficiently accelerated in the reverse shock to high energies. A weak magnetic field would not produce electrons energetic enough to produce gamma-rays (see Section 4.1). An electron to emit synchrotron radiation at a frequency ν needs an energy $E = 7.9(\nu/[\mathrm{GHz}])^{1/2}(B/[\mu\mathrm{G}])^{-1/2}$ GeV (e.g., Pacholczyk 1970), for $\nu = 1.4$ GHz in the ISM magnetic field $E \sim 4$ GeV. Hence, a strong radio signal at

these frequencies does not necessarily imply the presence of relativistic electrons capable of producing gamma radiation at energies higher than 10 GeV.

Another possibility that might decrease the synchrotron at 1.4 GHz without assuming a smaller power in relativistic particles is that the injected electrons have a steeper power-law index, i.e., $|\alpha| < 2$, as we learn from the previous section. With a steep injection the emission at long wavelengths decreases. A smaller value of $|\alpha|$ then would give a steeper photon distribution, decreasing the emission in the energy region of interest. However this effect is not expected to produce dramatic changes. It is worth mentioning that given the sensitivity of present observatories the lack of detection does not constitute a strong evidence for a lack of efficient particle acceleration in these sources.

The above analysis is made extrapolating the upper limits from a sample of five sources to all sources, and this might not be the general case. In particular, it does not apply to the case of BD +43°3654, which was in fact detected at radio. In this system the emission detected at 1.42 and 4.86 GHz is of the order of $\sim 10^{30}$ erg s^{-1}. Such a high luminosity is not even achieved for a higher value of the magnetic field strength (e.g., our $B_\star = 1$ kG model).

The upper limits at X-rays between 0.3 and 10 keV from previous works are between 10^{30} and 10^{31} erg s^{-1}; in the cases studied here, except the case with $B_\star = 1$ kG, the luminosity between 1 and 10 keV lies below these values. For these cases the analysis made in De Becker et al. (2017) still holds, which is as follows: current detectors are not able to differentiate between the nonthermal emission, if any, and the stellar thermal one. In the case of a high stellar magnetic field, the emission should be detectable at X-rays with present observatories. A lack of detection might indicate that such a large value for $B_\star$ is not reached in these objects or that the magnetic field in the wind is overestimated.

7. Concluding Remarks

In this work we study a very general case of a massive runaway star bow shock, assuming typical values for describing the system and ordinary assumptions. The strongest assumption that is made in our modeling is the acceleration of electrons through DSA in the wind shock. The only indirect evidence that supports this assumption is the observation of synchrotron emission from the bow shock of BD +43°3654. This hypothesis will be carefully analyzed in a future work.

In what follows we summarize the main conclusions of this study:

1. According to our model, the nonthermal emission produced in the bow shock of a massive runaway star is mainly made of synchrotron radiation and IC emission at gamma-rays, as predicted by previous works.
2. In the general case the luminosity predicted here at X-rays lies below the existing X-ray upper limits. In the case of a strong stellar magnetic field the synchrotron radiation is the dominant process at soft X-rays.
3. A fraction between 4×10^{-5} and 10^{-4} of the wind power is converted into IC radiation, with a maximum around $E = 100$ GeV.
4. A fraction between 9×10^{-6} and 10^{-4} of the wind power is converted into synchrotron emission, with a maximum around $E = 1$ eV.
5. Transport effects, advection and diffusion, dominate over radiation losses. Only $\sim 0.16\% - 0.4\%$ of the injected power in electrons is radiated; the bulk of the particles leave the system and radiate elsewhere.
6. Synchrotron emission from the bow shock tail, produced by dragged electrons, might be important, especially in the fast diffusion regime.
7. The bulk IC radiation is coming from the *cup* region of the bow shock.
8. The hadronic component in the SED is completely negligible; protons diffuse and advect into the ISM almost without losing energy.
9. Given the better sensibility of current instruments at radio wavelengths, these systems are more prone to be detected at radio through the synchrotron emission they produce than at gamma energies.
10. The lack of detection at radio of specific sources put stringent constraints on the emission expected at gamma-rays.

M.V.d.V. acknowledges support from the Alexander von Humboldt Foundation. The authors would like to thank Dr. Reinaldo Santos-Lima for fruitful discussions. We also thank the anonymous referee for insightful comments.

Software: PLUTO (Mignone et al. 2007).

ORCID iDs

M. Pohl https://orcid.org/0000-0001-7861-1707

References

Abdo, A. A., Ajello, M., Allafort, A., et al. 2013, ApJS, 208, 17
Acero, F., Ackermann, M., Ajello, M., et al. 2015, ApJS, 218, 23
Becker, R. H., White, R. L., & Helfand, D. J. 1995, ApJ, 450, 559
Bednarek, W., & Pabich, J. 2011, A&A, 530, A49
Benaglia, P., Romero, G. E., Martí, J., Peri, C. S., & Araudo, A. T. 2010, A&A, 517, L10
Berezinskii, V. S., Bulanov, S. V., Dogiel, V. A., & Ptuskin, V. S. 1990, Astrophysics of Cosmic Rays (Amsterdam: North-Holland)
Brose, R., Telezhinsky, I., & Pohl, M. 2016, A&A, 593, A20
Canto, J., Raga, A. C., & Wilkin, F. P. 1996, ApJ, 469, 729
Caprioli, D., & Spitkovsky, A. 2014, ApJ, 783, 91
Comeron, F., & Kaper, L. 1998, A&A, 338, 273
Condon, J. J., Cotton, W. D., Greisen, E. W., et al. 1998, AJ, 115, 1693
De Becker, M., del Valle, M. V., Romero, G. E., Peri, C. S., & Benaglia, P. 2017, MNRAS, 471, 4452
de la Cita, V. M., Bosch-Ramon, V., Paredes-Fortuny, X., Khangulyan, D., & Perucho, M. 2016, A&A, 591, A15
del Palacio, S., Bosch-Ramon, V., Müller, A. L., & Romero, G. E. 2018, arXiv:1806.10863
del Valle, M. V., Müller, A. L., & Romero, G. E. 2018, MNRAS, 475, 4298
del Valle, M. V., & Romero, G. E. 2012, A&A, 543, A56
del Valle, M. V., & Romero, G. E. 2014, A&A, 563, A96
del Valle, M. V., Romero, G. E., & De Becker, M. 2013, A&A, 550, A112
del Valle, M. V., Romero, G. E., & Santos-Lima, R. 2015, MNRAS, 448, 207
Dgani, R., van Buren, D., & Noriega-Crespo, A. 1996, ApJ, 461, 927
Draine, B. T. 2011, Physics of the Interstellar and Intergalactic Medium (Princeton, NJ: Princeton Univ. Press)
Draine, B. T., & Li, A. 2007, ApJ, 657, 810
Drury, L. O. 1983, RPPh, 46, 973
Ellison, D. C., Moebius, E., & Paschmann, G. 1990, ApJ, 352, 376
Gaisser, T. K. 1990, Cosmic Rays and Particle Physics (New York: Cambridge Univ. Press)
H.E.S.S. Collaboration, Abdalla, H., Abramowski, A., et al. 2018, A&A, 612, 12
Hoogerwerf, R., de Bruijne, J. H. J., & de Zeeuw, P. T. 2000, ApJL, 544, L133
Kobulnicky, H. A., Chick, W. T., Schurhammer, D. P., et al. 2016, ApJS, 227, 18
Kobulnicky, H. A., Gilbert, I. J., & Kiminki, D. C. 2010, ApJ, 710, 549

Lequeux, J. 2005, The Interstellar Medium (Berlin: Springer)
Longair, M. S. 2011, High Energy Astrophysics (Cambridge: Cambridge Univ. Press)
López-Santiago, J., Miceli, M., del Valle, M. V., et al. 2012, ApJL, 757, L6
Mac Low, M.-M., & Norman, M. L. 1993, ApJ, 407, 207
Meyer, D. M.-A., Mackey, J., Langer, N., et al. 2014, MNRAS, 444, 2754
Meyer, D. M.-A., Mignone, A., Kuiper, R., Raga, A. C., & Kley, W. 2017, MNRAS, 464, 3229
Meyer, D. M.-A., van Marle, A.-J., Kuiper, R., & Kley, W. 2016, MNRAS, 459, 1146
Mignone, A., Bodo, G., Massaglia, S., et al. 2007, ApJS, 170, 228
Mokiem, M. R., de Koter, A., Vink, J. S., et al. 2007, A&A, 473, 603
Nolan, P. L., Abdo, A. A., Ackermann, M., et al. 2012, ApJS, 199, 31
Pacholczyk, A. G. 1970, Radio Astrophysics. Nonthermal Processes in Galactic and Extragalactic Sources (San Francisco, CA: Freeman)
Pakmor, R., Pfrommer, C., Simpson, C. M., & Springel, V. 2016, ApJL, 824, L30
Pereira, V., López-Santiago, J., Miceli, M., Bonito, R., & de Castro, E. 2016, A&A, 588, A36
Peri, C. S., Benaglia, P., Brookes, D. P., Stevens, I. R., & Isequilla, N. L. 2012, A&A, 538, A108
Peri, C. S., Benaglia, P., & Isequilla, N. L. 2015, A&A, 578, A45
Pohl, M. 1993, A&A, 270, 91
Raga, A. C., Noriega-Crespo, A., Cantó, J., et al. 1997, RMxAA, 33, 73
Romero, G. E., Del Valle, M. V., & Orellana, M. 2010, A&A, 518, A12
Ryu, D., & Vishniac, E. T. 1987, ApJ, 313, 820
Sánchez-Ayaso, E., del Valle, M. V., Martí, J., Romero, G. E., & Luque-Escamilla, P. L. 2018, ApJ, 861, 32
Schulz, A., Ackermann, M., Buehler, R., Mayer, M., & Klepser, S. 2014, A&A, 565, A95
Telezhinsky, I., Dwarkadas, V. V., & Pohl, M. 2012, A&A, 541, A153
Tetzlaff, N., Neuhäuser, R., & Hohle, M. M. 2011, MNRAS, 410, 190
Toalá, J. A., Oskinova, L. M., González-Galán, A., et al. 2016, ApJ, 821, 79
Toalá, J. A., Oskinova, L. M., & Ignace, R. 2017, ApJL, 838, L19
van Buren, D., & McCray, R. 1988, ApJL, 329, L93
van Marle, A. J., Meliani, Z., Keppens, R., & Decin, L. 2011, ApJL, 734, L26
Voelk, H. J., & Forman, M. 1982, ApJ, 253, 188
Walder, R., Folini, D., & Meynet, G. 2012, SSRv, 166, 145
Wiersma, R. P. C., Schaye, J., & Smith, B. D. 2009, MNRAS, 393, 99
Wilkin, F. P. 1996, ApJL, 459, L31
Wilkin, F. P. 2000, ApJ, 532, 400